# Atomic layer restructuring of gold surfaces by N-heterocyclic carbenes over large surface areas

Eden Goodwin[1,2,‡], Matthew Davies[2,3,4,‡], Maram Bakiro[1,2], Emmett Desroche[2,5], Francesco Tumino[2,5], Mark Aloisio[2,5], Cathleen M. Crudden[2,5,*], Paul J. Ragogna[2,3,4,6,*], Mikko Karttunen[2,3,4,*], and Seán T. Barry[1,2,*]

1Department of Chemistry, Carleton University, Ottawa, Ontario, K1S 5B6, Canada
2Carbon to Metal Coating Institute, Queen's University, Kingston, Ontario, K7L 3N6, Canada
3Department of Physics and Astronomy, Western University, London, Ontario, N6A 3K7, Canada
4Department of Chemistry, Western University, London, Ontario, N6A 3K7, Canada
5Department of Chemistry, Queen's University, Kingston, Ontario, K7L 3N6, Canada
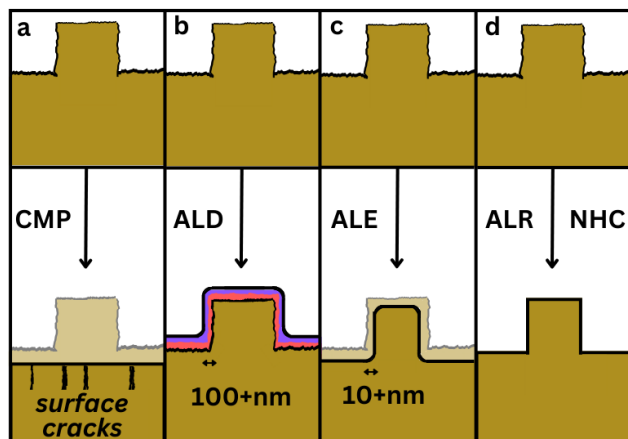6Surface Science Western, 999 Collip Cir, London, ON N6G 0J3, Canada

**ABSTRACT:** Even highly planar, polished metal surfaces display varying levels of roughness that can affect their optical and electronic properties, impacting performance in state-of-the-art microelectronics. Current methods for smoothing rough metallic surfaces require either the removal or addition of substantial amounts of material using complex processes that are incompatible with 3-dimensional nano-scale features needed for state-of-the-art applications. We present a vapor-phase process that results in up to a 60% smoothing of nanometer scale rough gold surfaces through a single exposure to a new class of ligand called N-heterocyclic carbenes (NHCs). This process does not require removal or addition of metal from the surface and provides smoothing at the Ångström scale. Smoothing occurs in a single deposition, giving quantifiable differences in the adsorption behavior of the resulting surfaces. The process takes place through an adatom–extraction-driven destabilization and restructuring of the surface in a self-limiting manner. This novel process is achieved without the use of harsh chemical etchants or mechanical intervention, takes only minutes, and can easily be integrated with vapor phase processing in situ. It offers a promising avenue for subnanometer smoothing in microfabrication workflows. Our observations pave the way for atomic layer restructuring (ALR), a technique that compliments atomic layer deposition (ALD) and atomic layer etching (ALE) in the fabrication and processing high precision materials.

Moore's law, that the number of transistors in an integrated circuit doubles approximately every two years, has held true for almost six decades. This law is now being challenged by the continual need to shrink the size of features on such devices. Current sizing is so small that we are approaching the Ångström Era–where feature size is set by the size of atoms.[1] As a practical consequence of these advances, the surface roughness of metals involved in interconnects and complex patterns must be controlled at the same level. With the exception of ideal single crystal surfaces, surface roughness is typically well outside limits needed for the Ångström Era.

Current methods to reduce roughness in metal films are shown in Figure 1. Chemical mechanical planarization (CMP) is the most common technique,[3] in which wafers are mechanically polished against a pad coated with a complex slurry of abrasives and chemically reagents to remove protruding features.[2] CMP is not a conformal process so it can only be used to smooth surface-facing features. Also, it introduces surface defects, deposits large amounts of debris on the surface, and is a costly process generating considerable waste.[4] Atomic layer deposition (ALD) and atomic layer etch (ALE) have been reported to smooth surfaces to the sub-nanometer scale in a conformal fashion (Fig. 1b, c).[5,6] ALD processes result in film growth through sequential self-limiting surface reactions, which produce a uniform coating across protruding and recessed features. As film thickness increases, valley walls grow together and force a reduction in surface roughness of between $5 \times 10^{-5}$ and $6 \times 10^{-4}$ nm/cycle.[7,8] Typically thousands of deposition cycles are needed to achieve a 1 nm reduction in roughness, corresponding to the deposition of over 100 nm of film.[6]

In ALE processes, sequential self-limiting surface reactions generate volatile species from the surface, preferentially etching high energy surface sites.[4] This results in a significantly larger smoothing effect, with roughness reduction occurring at a rate of $3 \times 10^{-3}$ nm/cycle.[9] Although more efficient than ALD, hundreds of etching cycles are still required to achieve a 1 nm reduction in roughness, removing more than 10 nm of film. While CMP, ALD, and ALE are effective to smooth surfaces, their additive or subtractive nature changes film thickness by 10s to 100s of nm, making them fundamentally incompatible with smoothing nanoscale features that are orders of magnitude smaller scales. Molecular adsorbates such as nitrate, chloride, thiolate or phosphine have been reported to destabilize metal surfaces leading to, for example, lifting the herringbone structure of Au(111), but these transformations have not been reported on macroscopic length scales,[10–12] nor can they integrate easily with common manufacturing processes.

N-Heterocyclic carbenes (NHCs) are new molecular adsorbates that have attracted considerable attention for their ability to form robust self-assembled monolayers on a variety of metal surfaces.[13,14] Their ability to form molecular complexes with a range of metals such as copper,[15] gold,[16] and others[17,18] has been mirrored in the formation of self-assembled monolayers on metal surfaces.[19–24] The strong adsorption energy of NHCs on metal surfaces has led to their use in a variety of applications,[23,25,26] including as small molecule inhibitors (SMIs) that protect metal surfaces during subsequent additive processes.[27] Importantly, the strength of the NHC-metal bond can lead to either partial or complete metal atom abstraction.[28,29] Depending on the nature of the metal and on NHC structure, this leads to incorporation of metal atoms in the overlayer structure, either bound to a single, upright NHC or in flat-lying $M(NHC)_2$ species.[28,29] In both cases, highly ordered surfaces result that contain metal atoms abstracted from the bulk. Herein, we leverage this concept by employing NHCs to convert metallic surfaces with levels of roughness commonly encountered in manufacturing processes to surfaces with subnanometer levels of smoothness. This atomic layer restructuring (ALR) process is demonstrated on surfaces with areas as large as 1.5 cm$^2$.

# Results and Discussion

Rough surfaces were generated by sputtering an Au(111) single crystal with a 3 µA current of Ar ions accelerated at 1.5 keV for five minutes. This method was chosen because the roughness of non-single crystal surfaces exceeded the height range of our scanning tunneling microscope (STM) and therefore our ability to image the surfaces. The roughened surface prepared from an Au(111) crystal (Figure 2a) was characterized by a root-mean-square (RMS) roughness of 0.77 ± 0.04 nm (n=10). These surfaces were then treated in the gas phase with iPrNHC, (Fig. 2), chosen because of its ubiquity in SAM formation and its ability to form ordered overlayers on metal single crystals.[13,29] After exposure to approximately 3 L of iPrNHC (Figure 2b), the RMS roughness dropped to 0.54 ± 0.04 nm (n=8), corresponding to a roughness reduction of 29 ± 6 %. Importantly, this roughness reduction affects both sides of the height distribution (Figure 2g), indicating that the effect is not restricted to removal of protruding features as would be expected in CMP approaches, but enables filling in of features with a "negative" height. STM imaging at a higher magnification (Figure 2c) shows the characteristic zig-zag pattern associated with a planar surface covered with iPrNHC.[29]

The surface density of protruding features was reduced following exposure to iPrNHC, underscoring the extensive nature of surface restructuring (see Methods for details). Although the radius of individual features remained constant within the margin of error (3.8 ± 0.5 nm before vs. 3.4 ± 0.3 nm after), the overall area of these features was reduced by 60 ± 10 % due to a reduction in surface density. The correlation length was seen to increase after exposure to NHC from 8.4 ± 0.2 nm to 10.5 ± 0.3 nm, indicating an average increase of the width of the crystal terraces, consistent with roughness reduction.

Local surface structure was quantified using the recently introduced mixed radial-angular 3-body distribution function (g3, see Figure S.1 for details).[13] In brief, g3 is a 3-body generalization of the traditional pair correlation function, and it is proportional to the probability of there being a feature at a given distance (r) and an angle (θ) from two reference features. The resulting g3 distribution provides a fingerprint for each conformation allowing for a visualization of the local structure, packing distance and orientation, as a contour plot. Before NHC exposure (Figure 2d), the features (islands) were observed to pack much more closely together than after exposure (Figure 2e).
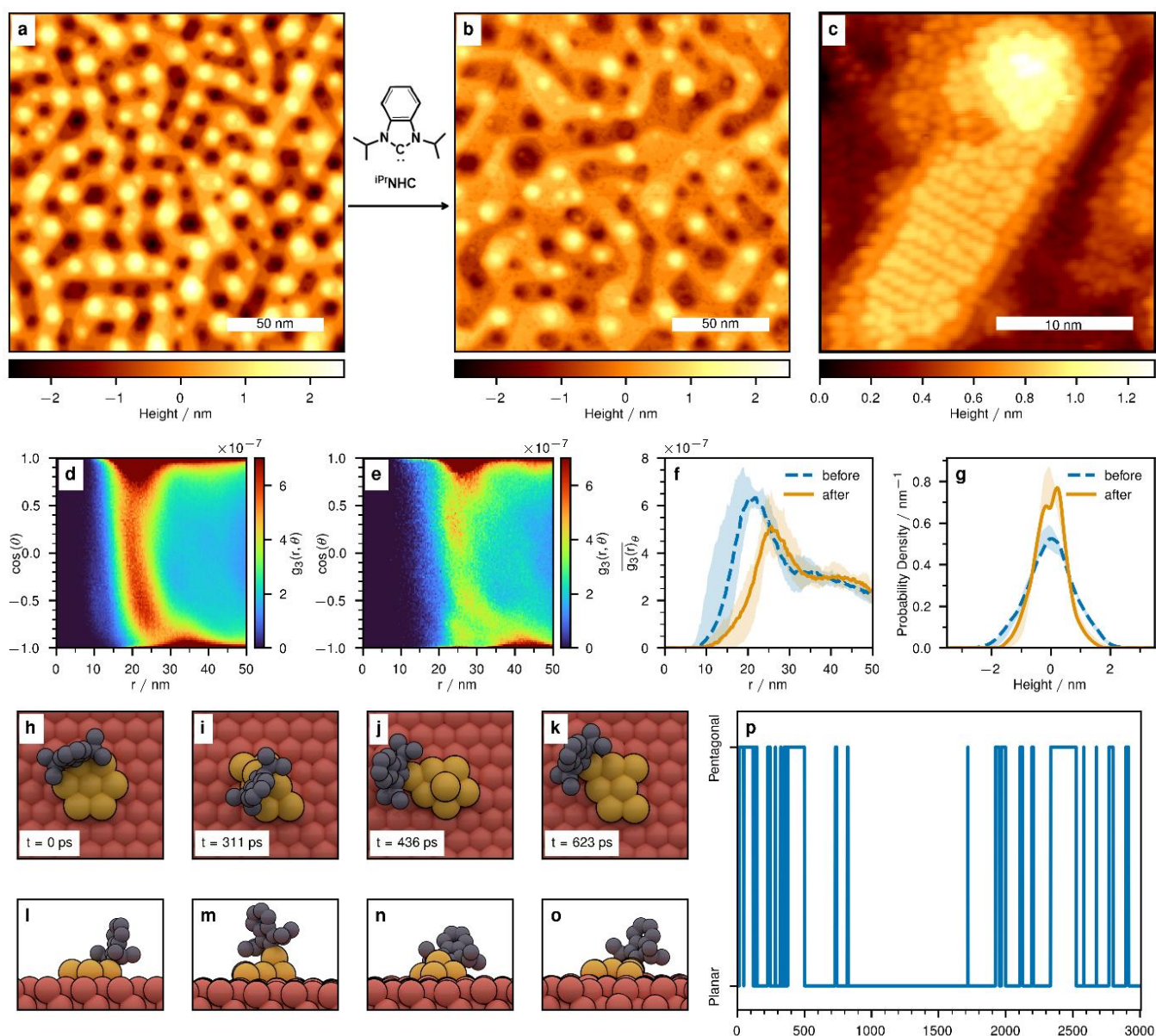
Averaging out the angular dimension (Figure 2f) clearly shows shifting of the most probable (maximum) radial packing distance from 21 ± 2 nm to 26 ± 1 nm. Alongside this increase in separation, orientational packing is altered. The high probability at $\cos(\theta) =$ 1 and –1 (0° and 180°) indicates a linear chain type motif both before and after exposure to NHC. Differences are apparent in the center of the distribution: before exposure to NHC, the chain structures are more tightly packed together alongside one another, which gives rise to the diffuse peak between $\cos(\theta) = -0.8$ and 0.5. The latter is much less prominent after NHC exposure and subsequent restructuring of the surface, showing a more open packing.

**Fig. 1 | Methods of smoothing atomically rough surfaces. a**, Chemical mechanical planarization removes material but introduces surface cracks. **b**, Additive deposition by ALD adds layers of material. **c**, Subtractive etching (ALE) works through repeated removal of layers of material. **d**, Atomic layer restructuring (ALR) employs molecular adsorbates, here N-heterocyclic carbenes (NHCs), which function by redistributing material unlike subtractive or additive processes.

Motivated by these observed smoothing and morphological changes, simulations were undertaken to understand the atomic-level physical mechanism(s) behind them. A series of molecular dynamics (MD) simulations of NHC-induced changes on model roughened gold surfaces were undertaken using the FLARE machine-learning force field that was trained using density-functional theory (DFT) calculations (see Figure S.2 for validation of the accuracy of the machine-learning force field).[30] Compared to this method, traditional force fields such as the GOLP force field family require restraining the positions of the gold atoms, which would preclude proper exploration of this system.[31]

The simulations revealed two key factors that provide insight into the mechanism of smoothing. Firstly, as observed on planar surfaces,[28] NHC molecules are freely able to abstract a metal atom from an island to form an NHC-adatom complex (Figures 2h-o). At no point in the simulations did the adatom is an irreversible extraction process similar to adatom extraction from a planar surface

**Fig. 2 | Atomic scale smoothing with a proposed mechanism. a,b**, 200 x 200 nm$^2$ STM images of the sputtered Au(111) surface before NHC treatment (**a**) and after (**b**). RMS surface roughness is 0.77 ± 0.04 nm before, and 0.54 ± 0.04 nm after exposure. c, Higher resolution 22.6 x 22.6 nm$^2$ STM image of the Au surface after NHC exposure, showing a molecular monolayer of NHC in its characteristic zig-zag self-assembly pattern. **d,e**, Radial-angular distribution function (g3) of the surface features before (**d**) and after (**e**) NHC exposure. **f**, g3 averaged over the radial dimension showing a shift in the radial peak location and intensity. g, Normalized height probability distributions of (**a**) and (**b**) are shown in blue and orange traces, respectively, the shaded region shows the minima and maxima for all areas imaged. NHC exposure makes the distribution narrower and sharper around zero, a clear signature of smoothing. **h-o**, Snapshots from MD simulations illustrating adatom-induced destabilization induced by NHC (grey) interaction with an island (gold) starting with the intact island (**h,l**), extracting an adatom (**i,m**), the island adopting a pentagonal state with a raised central atom (**j,n**), and returning to a planar state (**k,o**). The underlying surface is coloured red for contrast with the island. p, Speed of predicted transitions between the planar and pentagonal states.

that causes roughening.[28] DFT calculations place the adatom extraction energy, $E_{extraction} = E_{total} - E_{extracted}$ at -4 kJ/mol with an NHC, and 26 kJ/mol without the NHC, illustrating the strong effect of the NHC. Secondly, once extracted from the island, the mobility of the adatom itself and return to fill the gap left by its removal, underscoring that this the mobility of the remainder of the island increased because of the destabilization caused by the vacancy, and the interactions of the NHC-bound adatom with the edge of the island defect. Using g3 as a metric for clustering analysis (Figure S.3), two distinct island states were identified as having planar (Figures 2h, i, k) and a pentagonal conformation (Figure 2j), each with a different areal footprint (61 ± 1 Å$^2$ and 55 ± 1 Å$^2$, respectively). The destabilization caused by the NHC allowed the island to readily and rapidly switch between these two different conformational states (Figure 2p). This conformational switching behavior was not observed in the gold-only control simulations without an NHC. Without an NHC to extract an adatom, the island remained hexagonal and in the planar state, as might be expected
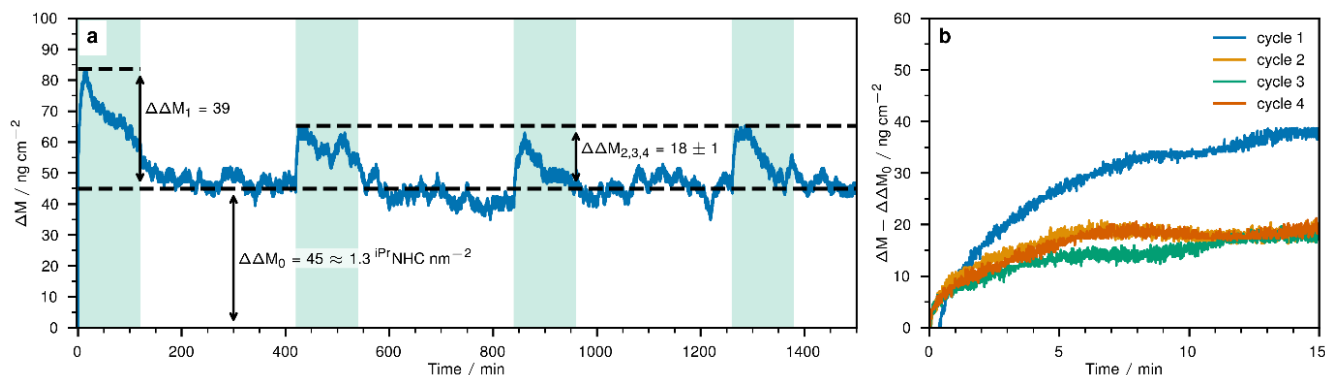
**Fig. 3 | Quartz crystal microbalance measurements of polished gold electrode after repeated NHC exposure. a**, QCM trace showing the change in areal mass density over time for cycled adsorption of NHC on an optically polished Au surface. **b**, The first 15 minutes of each cycle, measured from the persistent baseline ($\Delta\Delta M_0$), show rapid saturation and exemplify the difference between the first and subsequent cycles.

based on the large DFT-derived extraction energy. In the newly enabled pentagonal state (Figure 2j), island atoms were able to diffuse between the surface sites without requiring a concerted movement of the entire island. This pentagonal state corresponds to a smaller areal footprint due to the partial raising of the central atom accompanied by two of the edge atoms moving inwards (Figures 2j, n). Even in the planar state, the destabilization caused by the missing atom allowed for single atom diffusion around the edge of the island and moving the gap (Figure 2k) from where it was extracted (Figure 2h). Thus, a single NHC affects the mobility of not just the adatom it is bonded to, but also the mobility of the entire island.

Based on the STM data and computer simulations, we propose a mechanism for the smoothing process that relies on two key properties of NHCs: (i) their ability to abstract metal atoms; and, (ii) the self-assembly of NHC-bound adatoms into ordered monolayers. Upon adsorption onto a surface, NHCs disrupt the metal surface to an extent that can lead to the extraction of adatoms.[28,29] This extraction then destabilizes the surface through the formation of surface adsorbed NHC–adatom species. If the number of NHCs on the surface is below saturation coverage, these surface-bound NHC adatoms are mobile and able to diffuse across the surface. Depending on the surface concentration, different types of self-assembled monolayers are observed.[29] At high enough concentrations, ordered lattices are observed, in which extracted adatoms are dispersed on the surface as key components of the organometallic overlayer. An interesting outcome of this mechanism is that the degree of smoothing should be a function of the initial roughness. The rougher the initial surface, the higher the probability that adatom extraction to occur from an island compared to the terrace. This effect is likely to be magnified by the instability of atoms in islands compared to those in terraces.

To examine the applicability of this smoothing effect to large non-crystalline metal surfaces, we exposed polished gold electrodes to **iPr**NHC in a quartz crystal microbalance (QCM) set up.[9–11] These polished electrodes have a rougher surface than the artificially roughened system used for STM imaging. **iPr**NHC was introduced onto the polished gold electrode surface by repeated adsorption/desorption cycles and the differences in the adsorption mass of the first cycle was determined relative to subsequent cycles (Figures 3a and b). The adsorption of **iPr**NHC in the first deposition cycle resulted in a maximum mass gain of 84 ng·cm⁻², while the three subsequent deposition cycles were characterized by mass gains of 65 ± 1 ng·cm⁻². NHC loading in the first cycle corresponds to 2.49 **iPr**NHC·nm⁻², significantly higher than the planar single crystal surface coverage of 1.73 **iPr**NHC·nm⁻² previously reported,[29] and closer to what is observed on polycrystalline gold surfaces.[32] This initial mass loading relaxed to 45 ng·cm⁻² (1.30 **iPr**NHC·nm⁻²) through loss of physisorbed **iPr**NHC. This NHC coverage is similar to that observed for upright, strongly bound NHCs on single crystal Au(111) surfaces.[29] In all subsequent pulses during QCM measurements, the capacity for physisorption decreases to a constant level of 18 ± 1 ng·cm⁻², indicating that changes to the surface occurred in the initial exposure and in a self-limiting manner.

Adsorption kinetics followed a two-state model (Figure S.4), which likely correspond to fast chemisorption and slow, weakly bound physisorption events. The initial rougher surface has a larger effective surface area with a higher number of available binding sites than the smoothed surface after NHC exposure. Thus, the first pulse shows a much larger initial mass gain that relaxes during the purge by surface restructuring and loss of physisorbed NHC. The subsequent physisorbed mass gains were consistent and smaller in magnitude because of the decreased capacity for physisorption displayed by the restructured surface.

The ability to accomplish smoothing was next examined over macroscopic length scales. Spectroscopic ellipsometry (SE) was employed to measure smoothing of gold surfaces across 1.54 cm², the area of the QCM crystals, before and after NHC exposure (Figure 4). Surface mapping of 149 points across three different crystals showed more intense smoothing for surfaces that had higher initially roughness, consistent with our proposed mechanism. The degree of smoothing was quantified by determining the smoothing factor (S) as $S=(1-R_{smooth}/R_{rough})$, where $R_{smooth}$ is the roughness after and $R_{rough}$ before the smoothing process determined by the SE-modelling (Figure 4d). Across these three samples, the smoothing factor varied depending on the initial surface roughness. The values ranged between 0.37 ± 0.04 to 0.66 ± 0.03 upon NHC exposure. This trend is consistent with the smoothing observed in the STM experiments (0.29 ± 0.06) calculated using the RMS roughness. This comprehensive surface mapping approach demonstrates that smoothing occurs uniformly on the macroscopic scale.

Assuming a linear trend at low roughness values, a limit of smoothing can be estimated as the intercept between the linear fit of the data and y=x (Figure S.5), the point of the line where the initial roughness would not be reduced any further, and beyond which the surface is roughened. This model predicts that surfaces with an initial roughness of 3.3 ± 1.2 Å or lower will not experience smoothing and may instead be roughened through exposure to **iPr**NHC. This predicted boundary is similar to the Au surface
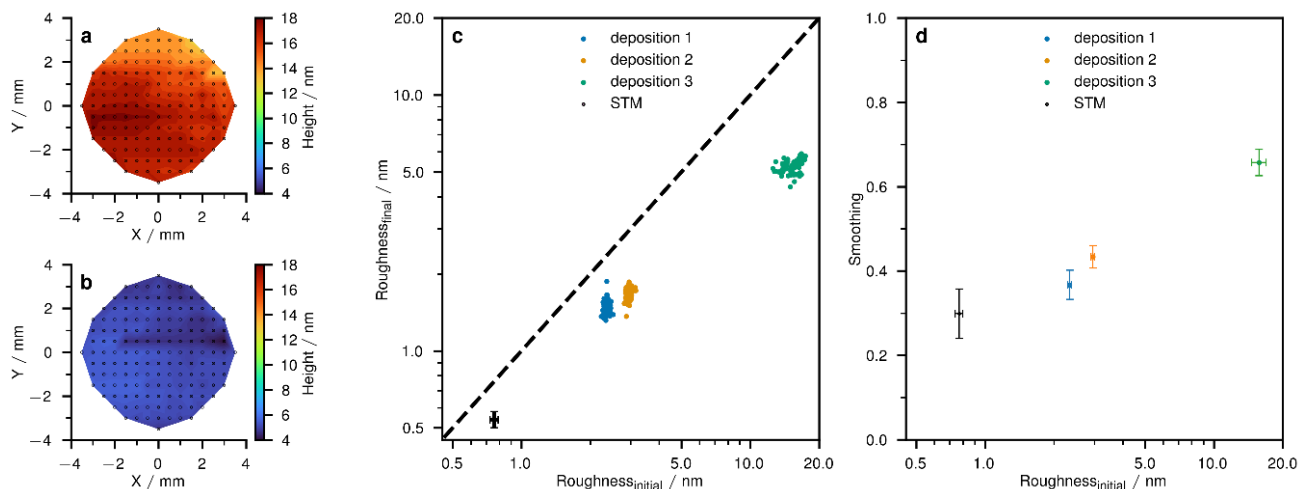
**Fig. 4 | Macroscale smoothing with a comparison to the atomic scale. a,b** Topographical mapping of surface roughness of an optically polished Au electrode on top of a quartz crystal before (**a**) and after (**b**) exposure to iPrNHC. Black dots indicate the sampling points across the surface. **c**, Comparison of the roughness before and after NHC exposure for three quartz crystals on a log-log scale, where the black dashed line indicates no smoothing. **d**, The smoothing factor shows that while all samples were smoothed, the degree of smoothing increases with increasing initial roughness. The RMS roughness determined from STM has been included in (**c**) and (**d**) alongside the rougher spectroscopy ellipsometry systems to show the difference in scales of the systems.

roughness achievable either through CMP (3.8 ± 0.5 Å)[33] or pressure-forming template stripping (3.5 ± 0.5 Å)[34], but in our case is attainable without any mechanical intervention.

# Methods

*Scanning Tunnelling Microscopy*

STM experiments were performed under ultra-high vacuum (UHV) using a Createc LT-SPM system. An Au(111) single crystal (Mateck GmbH, Germany) was cleaned by several cycles of Ar sputtering and annealing to 575 °C. Before depositing iPrNHC, the surface was artificially roughened by sputtering it for 5 minutes with a 3 μA current of Ar ions accelerated at 1.5 keV. iPrNHC was deposited on the surface at room temperature via evaporation of hydrogen carbonate precursor iPrNHC•$H_2CO_3$, prepared by known methods,[35] using a custom-built evaporator. The inner cell of the evaporator hosts a p-doped Si substrate bridging two tungsten electrodes. The precursor was first dissolved in ethanol at a concentration of a 80 mmol/L. Then, a single drop of the solution was placed on the Si substrate and let dry in vacuum. The evaporation was performed by heating the Si substrate in line-of-sight with the Au surface with a 3 A current for 5 s. STM constant-current images were acquired at 77 K using a Pt/Ir tip. All STM images were acquired using an applied bias of 250 mV and a tunneling current setpoint of 20 pA. Selected images were plane-corrected and analysed using the Gwyddion software[36]. Large scale STM images (200 nm x 200 nm) were acquired to determine the local surface roughness. Repeated measurements on macroscopically separated areas were performed to statistically infer the global surface roughness.

*Machine Learning Force Field*

The Fast Learning of Atomistic Rare Events (FLARE) machine learning interatomic potential of Vandermause et al.[30] was applied to study the dynamic behaviour of a defect containing planar Au(111) surface interacting with an NHC. FLARE, introduced in 2022, is based on adaptive Bayesian inference, active learning, and Gaussian process regression. It uses density-functional theory (DFT) calculations for generating accurate force fields for molecular dynamics (MD) simulations (see also Figure S.2).

A B2 atomic cluster expansion (ACE) expansion descriptor[37] with 8 radial and 3 angular functions was used with a quadratic cutoff function, Chebyshev radial basis and a cutoff of 5 Å between all atomic species. The Sparse Gaussian Process (SGP) used a normalized dot product kernel[30] with integer power, ξ, equal to 2, and the energy scale hyperparameter, σ, initially set to 2 eV. The power corresponds to a five-body model. To train the FLARE force field, DFT calculations were undertaken using the projector augmented-wave (PAW) method as implemented in the GPAW software[38,39]. The Perdew-Burke-Ernzerhof (PBE) functional[40] was used with a plane wave cutoff of 300 eV sampling the Γ-point. Representative atomic environments were sampled through on-the-fly (OTF) active learning of various systems[41]. These systems included bulk Au, an Au(111) surface for initial training, alongside representative small island surfaces with a nearby NHC. The slabs in these systems consisted of 5 x 6 x 4 atoms, and featured either no adatoms, a single adatom, or a seven-atom hexagonal island cluster, deemed a stable structure from preliminary simulations of on surface aggregation.

These OTF systems were generated with new conformations added to the training set when the Gaussian process uncertainty of the atomic environment descriptor exceed a threshold of 0.01 (for Au-only systems) or 0.1 (for the NHC systems system). The different magnitude of these values is due to the different number of atomic species in the systems, these were chosen based avoiding excessive DFT calls, whilst still maintaining a reasonable configurational accuracy. The 4 trainable hyperparameters were the energy scale, σ, and the energy, force and stress noise scaling factors. The three noise parameters indirectly alter the training threshold by acting as a scaling factor.

OTF simulations were undertaken using the atomic simulation environment (ASE)[42]. A time step of 0.001 ps was used for the systems containing NHCs, and sampling was accelerated in systems consisting only of Au atoms by using an increased time step of 0.005 ps. This longer time step was possible due to the lack of light atoms. OTF training simulations were performed at 373 K. All training simulations were undertaken in the canonical (NVT) ensemble using the Berendsen thermostat[43].

Sampling was considered complete once test simulations, following the production simulation workflow below but using the smaller system sizes of the OTF training, never exceeded the 0.1 uncertainty threshold, otherwise, additional OTF training was performed starting from the failing configurations. A total of 338 individual DFT calculations were included in the final training set.

*Production Simulations*

The SGP was converted to a Mapped Gaussian Process (MGP), and the MGP-MD simulations were undertaken using the LAMMPS software.[44] A timestep of 1 fs was used, and configurations were saved every 250 fs. Larger systems (1120 and 1087 atoms, with and without an NHC, respectively) were generated consisting of a planar surface of consisting of a slab with dimensions of 15 × 18 × 4 atoms, with a small island and NHC generated on top. A hexagonal island arrangement of 7 atoms was built, determined as a stable structure from simulations of isolated adatoms aggregating on the surface.

The systems were initialized with velocities drawn from a Gaussian distribution[45,46] with an initial temperature of 70 K. All production simulations were run in the isobaric-isothermal ensemble (NPT) coupled using a Nosé-Hoover style thermostat and barostat,[47–49] coupled in the xy-plane to a 1 bar pressure with damping parameter of 100 fs and 1000 fs for the thermostat and barostat, respectively. All simulations were annealed from 70 K to the production temperature across a 10 ps window before data collection occurred. The production simulations were run for 3 ns.

*Computational Analysis*

Analyses of the MD trajectories was undertaken using in-house Python scripts with the MDAnalysis library.[50,51] To analyse the defect island conformational changes without a priori assumptions of the nature of any conformational changes, we applied the unsupervised machine learning method of Davies et al.[52] In brief, the method uses a mixed radial, angular three-particle correlation function (g3)[53] as the basic metric. The g3 function measures the local structure of the island atoms, and the resulting distribution provides a fingerprint each conformation; g3 distributions were measured across the time series of the simulation, taking windows of 1.25 ps.

Each of these distributions had its similarity compared with all other distributions using the structural similarity index metric (SSIM)[54] to create a similarity matrix. Each row of the symmetric SSIM matrix represents a vector comparing how similar the given distribution is to the set of all distributions. This (2400×2400)-dimensional matrix had its dimensions reduced into 2D using t-distributed stochastic neighbour embedding (t-SNE)[55] with random initialization. Density-Based Spatial Clustering of Applications with Noise (DBSCAN)[56] was then used to cluster this resulting data. An independent 2D dimensionality reduction of the similarity matrix using principal component analysis (PCA) was performed, and the clusters from the t-SNE/DBSCAN clustering were mapped onto the PCA projection to confirm the spatial separation of the clusters and to validate the clustering workflow.

The footprint of the surface island was defined as the area in the xy-plane occupied by the convex hull fitted around the atomic positions on the atoms, each atom represented as a circle with radius 1.66 Å. Calculation of this was over the same 1.25 ps windows as above with each point being the average of 5 values within that window.

*In situ Quartz Crystal Microbalance (QCM) monitoring*

In situ cycled adsorption studies were undertaken to determine the kinetics, degree of saturation, and binding modalities of the iPrNHC molecular layers on gold surfaces. All QCM measurements were conducted in a house-built hot-walled tube furnace reactor using an in situ QCM (Colnatec, EON-LT) with a built-in thermocouple, using 6 MHz AT-cut crystals with optically polished Au electrodes supplied from Philliptech. Carrier gas lines were heated to the deposition temperature to maintain isothermal conditions on the crystal surface. The temperature across the data acquisition time was recorded at 0.1 K intervals by the thermocouple and was normally distributed with a mean temperature of 374.67 K and standard deviation of 0.06 K. Data were logged at a frequency of approximately 10 points per second, recorded at 1 second accuracy.

Precursor was delivered using a pass-through style bubbler to maximize delivery to the surface. The bubbler was loaded with 100-200 mg of N,N-diisopropylbenzimidizolium bicarbonate salt within a nitrogen filled (99.998% purity) glovebox and sealed using a 2.75" ConFlat copper gasket. The bubbler was then attached using silver-plated VCR gaskets. Subsequently, the headspace of the bubbler was evacuated under no-flow (0 sccm) and room temperature conditions to prevent loss of precursor, after which the reactor was passivated using a standard alumina deposition (0.1 s $Al(CH_3)_3$, 30 s purge, 0.1 s $H_2O$, 20 s purge, 100 cycles). After this, a fresh crystal was installed within the reactor and then left to bake out overnight (18 hr) under process temperature (100 °C) and a low flow (5 sccm) of carrier gas (99.999% $N_2$) to remove any residual moisture and to allow the crystal to equilibrate.

In an adsorption experiment, fresh and equilibrated QCM crystals were exposed to a number of cycles (1 or 4) of a long dose (2 hr) of precursor from the heated (70 °C) bubbler under a flow (50 sccm) of carrier gas (99.999% $N_2$) at 100 °C followed by a long purge (5 hr) of carrier gas at the same temperature and flow rate. Following the cycled exposure of iPrNHC the crystal was left under purge conditions until 28 hours had elapsed from the beginning of the experiment, at which time the crystal was removed for ex-situ analysis by spectroscopic ellipsometry.

Recorded frequency change, Δf, was converted to areal mass density change, ΔM, using the Sauerbrey equation[57]:

$$\Delta M = \frac{\Delta m}{A} = \frac{\sqrt{(\rho_q \cdot \mu_q)}}{2f_0^2} \Delta f \qquad \text{(Equation 1)}$$

where Δm is the modelled change in mass across the surface of the piezo crystal, A is its surface area, $f_0$ the resonant frequency, $\rho_q$ the quartz density, and $\mu_q$ the quartz shear modulus. Using $f_0$ = 6 MHz, $\rho_q$ = 2.648 g cm$^{-3}$, and $\mu_q$ = 2.947 × 1011 g cm-1 s−2 yielded $\frac{\sqrt{\rho_q \cdot \mu_q}}{2f_0^2}$ = −12.27 ng cm$^{-2}$ Hz$^{-1}$

Spectroscopic Ellipsometry

The Effective Medium Approximation (EMA) was employed to model the surface roughness on a gold-coated QCM surface, both before and after the deposition of an iPrNHC monolayer. The QCM surface mapping and iPrNHC deposition were both performed in a cleanroom facility (class 100 – 10,000) to avoid surface contamination. The deposition of the iPrNHC monolayer was carried out in a PICOSUN R-200 advanced plasma enhanced ALD system. To ensure consistent surface roughness mapping before and after deposition, a scratch was made on the edge of the gold-coated QCM surface, aligned with a mark on the ellipsometry stage to maintain the same orientation during measurements.

Data were collected using an RC2 Spectroscopic Ellipsometer (SE) (J.A. Woollam Co.) with an incidence angle of 70° and wavelengths ranging from 200 to 2500 nm. Ellipsometry mapping was conducted across the sample surface before and after deposition. The SE scan created a uniform map of 149 points across the surface.

The modelling utilized CompleteEASE software (version 6.71a), which incorporates built-in EMA functions for surface roughness. The EMA functions within CompleteEASE utilize a 50:50 mix of optical constants. The optical model was configured with a built-in gold substrate with no additional layers. The "Include Surface Roughness" option in CompleteEASE was enabled, modelling the surface roughness as a 50:50 mix of the gold substrate and void (with optical constants; refractive index n=1 and extinction coefficient k=0).

Initial mapping was conducted to establish the baseline surface roughness of the gold-coated QCM substrate. Final mapping of the surface roughness was conducted under identical conditions to the initial mapping. Post-deposition surface roughness was modelled again using the EMA in CompleteEASE software.

# Conclusions

Treatment of roughened gold surfaces with organic molecular adsorbates, specifically N-heterocyclic carbenes, is shown to decrease surface roughness to the nanometer and Ångström scales. NHC-based smoothing can be accomplished across surfaces with centimeter–scale surface areas. The process takes place in seconds to minutes at room temperature after gas phase exposure to the NHC. A physical mechanism is proposed for this smoothing based on the known ability of NHCs to abstract and restructure adatoms from metal surfaces. When adatoms extraction occurs from surface islands, a destabilization is induced in the island that then facilitates surface smoothing by enhancing the mobility of the entire island. Unlike smoothing driven by additive ALD or subtractive ALE, this atomic layer restructuring (ALR) process offers a unique and new tool for the processing of gold surfaces, where the amount of metal on the substrate remains constant. This finding showcases the suitability of NHCs as subnanometer-scale small molecule atomic smoothing agents, providing the groundwork for the use of small molecule smoothing agents as promising alternatives for planarization as microelectronics manufacturing enters the Ångström age.

## AUTHOR INFORMATION

### Corresponding Authors

*Seán T. Barry: seanbarry@carleton.ca
*Paul J Ragogna: pragogna@uwo.ca
*Mikko Karttunen: mkarttu@uwo.ca
*Cathleen M. Crudden: cruddenc@chem.quensu.ca

### Author Contributions

The manuscript was written through contributions of all authors. All authors have given approval to the final version of the manuscript.  ‡These authors contributed equally.

### Notes

Supplementary information is available with online version of this article. Simulation parameters are available at www.github.com/softsimu/nhc. Correspondence and requests for materials should be addressed to C.M.C., P.J.R., M.K. and S.T.B.

## ACKNOWLEDGMENT

## ABBREVIATIONS

ALD: Atomic Layer Deposition
ALE: Atomic Layer Etching
ALR: Atomic Layer Restructuring
CMP: Chemical Mechanical Planarization
CVD: Chemical Vapour Deposition
DFT: Density Functional Theory
MD: Molecular Dynamics
NHC: N-Heterocyclic Carbenes
QCM: Quartz Crystal Microbalance
SE: Spectroscopic Ellipsometry
STM: Scanning Tunneling Microscopy

## REFERENCES

1. Martínez-Blanco, J.; Nacci, C.; Erwin, S. C.; Kanisawa, K.; Locane, E.; Thomas, M.; von Oppen, F.; Brouwer, P. W.; Fölsch, S. Gating a Single-Molecule Transistor with Individual Atoms. Nat. Phys. 2015, 11 (8), 640–644. https://doi.org/10.1038/nphys3385.

2. Jayachandran, D.; Sakib, N. U.; Das, S. 3D Integration of 2D Electronics. Nat. Rev. Electr. Eng. 2024, 1 (5), 300–316. https://doi.org/10.1038/s44287-024-00038-5.

3. Krishnan, M., Nalaskowski, J. W. & Cook, L. M. Chemical mechanical planarization: slurry chemistry, materials, and mechanisms. Chem. Rev. 110, 178–204 (2010).

4. Noman, E. A.; Ali Al-Gheethi, A.; Al-Sahari, M.; Yashni, G.; Mohamed, R. M. S. R.; Soon, C. F.; Nguyen, H.-H. T.; Vo, D.-V. N. An Insight into Microelectronics Industry Wastewater Treatment, Current Challenges, and Future Perspectives: A Critical Review. Appl. Water Sci. 2024, 14 (4), 64. https://doi.org/10.1007/s13201-024-02104-7.

5. George, S. M. Mechanisms of thermal atomic layer etching. Acc. Chem. Res. 53, 1151–1160 (2020).

6. Gerritsen, S. H. et al. Surface smoothing by atomic layer deposition and etching for the fabrication of nanodevices. ACS Appl. Nano Mater. 5, 18116–18126 (2022).

7. Elam, J. W., Sechrist, Z. A. & George, S. M. ZnO/Al$_2$O$_3$ nanolaminates fabricated by atomic layer deposition: growth and surface roughness measurements. Thin Solid Films 414, 43–55 (2002).

8. Myers, T. J. et al. Smoothing surface roughness using Al$_2$O$_3$ atomic layer deposition. Appl. Surf. Sci. 569, 150878 (2021).

9. Zywotko, D. R., Faguet, J. & George, S. M. Rapid atomic layer etching of Al$_2$O$_3$ using sequential exposures of hydrogen fluoride and trimethylaluminum with no purging. J. Vac. Sci. Technol. A 36, 061508 (2018).

10. Jewell, A. D., Tierney, H. L. & Sykes, E. C. H. Gently lifting gold's herringbone reconstruction: trimethylphosphine on Au(111). Phys. Rev. B 82, 205401 (2010).

11. Gao, W. et al. Chlorine adsorption on Au(111): chlorine overlayer or surface chloride? J. Am. Chem. Soc. 130, 3560–3565 (2008).

12. Driver, S. M., Zhang, T. & King, D. A. Massively cooperative adsorbate-induced surface restructuring and nanocluster formation. Angew. Chem. Int. Ed. 46, 700–703 (2007).

13. Smith, C. A. et al. N-Heterocyclic Carbenes in Materials Chemistry. Chem. Rev. 119, 4986–5056 (2019).

14. Kaur, G.; Thimes, R. L.; Camden, J. P.; Jenkins, D. M. Fundamentals and Applications of N-Heterocyclic Carbene Functionalized Gold Surfaces and Nanoparticles. Chem. Commun. 2022, 58 (95), 13188–13197. https://doi.org/10.1039/D2CC05183D.

15. Hagen, D. J.; Povey, I. M.; Rushworth, S.; Wrench, J. S.; Keeney, L.; Schmidt, M.; Petkov, N.; Barry, S. T.; Coyle, J. P.; Pemble, M. E. Atomic Layer Deposition of Cu with a Carbene-Stabilized Cu(I) Silylamide. J. Mater. Chem. C 2014, 2 (43), 9205–9214. https://doi.org/10.1039/C4TC01418A.

16. Griffiths, M. B. E. et al. Surfactant directed growth of gold metal nanoplates by chemical vapor deposition. Chem. Mater. 27, 6116–6124 (2015).

17. Hopkinson, M. N.; Richter, C.; Glorius, F. An Overview of N-Heterocyclic Carbenes. Nature 2014, 510, 485–496. https://doi.org/10.1038/nature13384.

18. Vivancos, Á., Segarra, C. & Albrecht, M. Mesoionic and related less heteroatom-stabilized N-heterocyclic carbene complexes: synthesis, catalysis, and other applications. Chem. Rev. 118, 9493–9586 (2018).

19. Crudden, C. M.; Horton, J. H.; Ebralidze, I. I.; Zenkina, O. V.; McLean, A. B.; Drevniok, B.; She, Z.; Kraatz, H. B.; Mosey, N. J.; Seki, T.; Keske, E. C.; Leake, J. D.; Rousina-Webb, A.; Wu, G. Ultra Stable Self-Assembled Monolayers of N-Heterocyclic Carbenes on Gold. Nat. Chem. 2014, 6 (5), 409–414. https://doi.org/10.1038/nchem.1891.

20. Zeng, Y.; Zhang, T.; Narouz, M. R.; Crudden, C. M.; McBreen, P. H. Generation and Conversion of an N-Heterocyclic Carbene on Pt(111). Chem. Commun. 2018, 54 (88), 12527–12530. https://doi.org/10.1039/C8CC06894A.

21. DeJesus, J. F., Trujillo, M. J., Camden, J. P. & Jenkins, D. M. N-Heterocyclic Carbenes as a Robust Platform for Surface-Enhanced Raman Spectroscopy. J. Am. Chem. Soc. 140, 1247–1250 (2018).

22. MacLeod, M. J.; Goodman, A. J.; Ye, H.-Z.; Nguyen, H. V.-T.; Van Voorhis, T.; Johnson, J. A. Robust Gold Nanorods Stabilized by Bidentate N-Heterocyclic-Carbene–Thiolate Ligands. Nat. Chem. 2019, 11 (1), 57–63. https://doi.org/10.1038/s41557-018-0159-8.

23. Berg, I., Amit, E., Hale, L., Toste, D. F. & Gross, E. N-heterocyclic carbene based nanolayer for copper film oxidation mitigation. Angew. Chem. 61, (2022).

24. Zhang, T.; Khomane, S. B.; Singh, I.; Crudden, C. M.; McBreen, P. H. N-Heterocyclic Carbene Adsorption States on Pt(111) and Ru(0001). Phys. Chem. Chem. Phys. 2024, 26 (5), 4083–4090. https://doi.org/10.1039/D3CP03539E.

25. Singh, I.; Lee, D. S.; Huang, S.; Bhattacharjee, H.; Xu, W.; McLeod, J. F.; Crudden, C. M.; She, Z. N-Heterocyclic Carbenes Meet Toll-like Receptors. Chem. Commun. 2021, 57 (68), 8421–8424. https://doi.org/10.1039/D1CC03030B.

26. Kang, S., Byeon, S. E. & Yoon, H. J. N-heterocyclic carbene anchors in electronics applications. Bull. Korean Chem. Soc. 42, 712–723 (2021).

27. Lomax, J. T.; Goodwin, E.; Aloisio, M. D.; Veinot, A. J.; Singh, I.; Shiu, W.-T.; Bakiro, M.; Bentley, J.; DeJesus, J. F.; Gordon, P. G.; Liu, L.; Barry, S. T.; Crudden, C. M.; Ragogna, P. J. Deposition of N-Heterocyclic Carbenes on Reactive Metal Substrates—Applications in Area-Selective Atomic Layer Deposition. Chem. Mater. 2024, 36 (11), 5500–5507. https://doi.org/10.1021/acs.chemmater.4c00412.

28. Wang, G.; Rühling, A.; Amirjalayer, S.; Knor, M.; Ernst, J. B.; Richter, C.; Gao, H.-J.; Timmer, A.; Gao, H.-Y.; Doltsinis, N. L.; Glorius, F.; Fuchs, H. Ballbot-Type Motion of N-Heterocyclic Carbenes on Gold Surfaces. Nat. Chem. 2017, 9 (2), 152–156. https://doi.org/10.1038/nchem.2622.

29. Inayeh, A.; Groome, R. R. K.; Singh, I.; Veinot, A. J.; De Lima, F. C.; Miwa, R. H.; Crudden, C. M.; McLean, A. B. Self-Assembly of N-Heterocyclic Carbenes on Au(111). Nat. Commun. 2021, 12 (1), 4034. https://doi.org/10.1038/s41467-021-23940-0.

30. Vandermause, J., Xie, Y., Lim, J. S., Owen, C. J. & Kozinsky, B. Active learning of reactive bayesian force fields applied to heterogeneous catalysis dynamics of H/Pt. Nat. Commun. 13, 5183 (2022).

31. Iori, F.; Di Felice, R.; Molinari, E.; Corni, S. GolP: An atomistic force-field to describe the interaction of proteins with Au(111) surfaces in water. J. Comput. Chem. 2009, 30 (9), 1465–1476. https://doi.org/10.1002/jcc.21165.

32. Qi, L.; Mayall, R. M.; Lee, D. S.; Smith, C.; Woods, A.; Narouz, M. R.; Hyla, A.; Bhattacharjee, H.; She, Z.; Crudden, C. M.; Birss, V. I. Energetics and Redox Kinetics of Pure Ferrocene-Terminated N-Heterocyclic Carbene Self-Assembled Monolayers on Gold. Langmuir 2024, 40 (33), 17161–17844. https://doi.org/doi/10.1021/acs.langmuir.4c01446.

33. Miller, M. S., Ferrato, M.-A., Niec, A., Biesinger, M. C. & Carmichael, T. B. Ultrasmooth gold surfaces prepared by chemical mechanical polishing for applications in nanoscience. Langmuir 30, 14171–14178 (2014).

34. Rubio-Lara, J. A., Bergler, F., Attwood, S. J., Edwardson, J. M. & Welland, M. E. Ultraflat gold QCM electrodes fabricated with pressure-forming template stripping for protein studies at the nanoscale. Langmuir 35, 8889–8895 (2019).

35. Crudden, C. M.; Horton, J. H.; Narouz, M. R.; Li, Z.; Smith, C. A.; Munro, K.; Baddeley, C. J.; Larrea, C. R.; Drevniok, B.; Thanabalasingam, B.; McLean, A. B.; Zenkina, O. V.; Ebralidze, I. I.; She, Z.; Kraatz, H. B.; Mosey, N. J.; Saunders, L. N.; Yagi, A. Simple Direct Formation of Self-Assembled N-Heterocyclic Carbene Monolayers on Gold and Their Application in Biosensing. Nat. Commun. 2016, 7 (1), 1–7. https://doi.org/10.1038/ncomms12654.

36. Nečas, D.; Klapetek, P. Gwyddion: An Open-Source Software for SPM Data Analysis. Open Phys. 2012, 10 (1), 181–188. https://doi.org/10.2478/s11534-011-0096-2.

37. Drautz, R. Atomic Cluster Expansion for Accurate and Transferable Interatomic Potentials. Phys. Rev. B 2019, 99 (1), 014104. https://doi.org/10.1103/PhysRevB.99.014104.

38. Mortensen, J. J.; Hansen, L. B.; Jacobsen, K. W. Real-Space Grid Implementation of the Projector Augmented Wave Method. Phys. Rev. B 2005, 71 (3), 035109. https://doi.org/10.1103/PhysRevB.71.035109.

39. Enkovaara, J.; Rostgaard, C.; Mortensen, J. J.; Chen, J.; Dułak, M.; Ferrighi, L.; Gavnholt, J.; Glinsvad, C.; Haikola, V.; Hansen, H. A.; Kristoffersen, H. H.; Kuisma, M.; Larsen, A. H.; Lehtovaara, L.; Ljungberg, M.; Lopez-Acevedo, O.; Moses, P. G.; Ojanen, J.; Olsen, T.; Petzold, V.; Romero, N. A.; Stausholm-Møller, J.; Strange, M.; Tritsaris, G. A.; Vanin, M.; Walter, M.; Hammer, B.; Häkkinen, H.; Madsen, G. K. H.; Nieminen, R. M.; Nørskov, J. K.; Puska, M.; Rantala, T. T.; Schiøtz, J.; Thygesen, K. S.; Jacobsen, K. W. Electronic Structure Calculations with GPAW: A Real-Space Implementation of the Projector Augmented-Wave Method. J. Phys. Condens. Matter 2010, 22 (25), 253202. https://doi.org/10.1088/0953-8984/22/25/253202.

40. Perdew, J. P.; Burke, K.; Ernzerhof, M. Generalized Gradient Approximation Made Simple. Phys. Rev. Lett. 1996, 77 (18), 3865–3868. https://doi.org/10.1103/PhysRevLett.77.3865.

41. Vandermause, J.; Torrisi, S. B.; Batzner, S.; Xie, Y.; Sun, L.; Kolpak, A. M.; Kozinsky, B. On-the-Fly Active Learning of Interpretable Bayesian Force Fields for Atomistic Rare Events. Npj Comput. Mater. 2020, 6 (20). https://doi.org/10.1038/s41524-020-0283-z.

42. Hjorth Larsen, A.; Jørgen Mortensen, J.; Blomqvist, J.; Castelli, I. E.; Christensen, R.; Dułak, M.; Friis, J.; Groves, M. N.; Hammer, B.; Hargus, C.; Hermes, E. D.; Jennings, P. C.; Bjerre Jensen, P.; Kermode, J.; Kitchin, J. R.; Leonhard Kolsbjerg, E.; Kubal, J.; Kaasbjerg, K.; Lysgaard, S.; Bergmann Maronsson, J.; Maxson, T.; Olsen, T.; Pastewka, L.; Peterson, A.; Rostgaard, C.; Schiøtz, J.; Schütt, O.; Strange, M.; Thygesen, K. S.; Vegge, T.; Vilhelmsen, L.; Walter, M.; Zeng, Z.; Jacobsen, K. W. The Atomic Simulation Environment—a Python Library for Working with Atoms. J. Phys. Condens. Matter 2017, 29 (27), 273002. https://doi.org/10.1088/1361-648X/aa680e.

43. Berendsen, H. J. C.; Postma, J. P. M.; van Gunsteren, W. F.; DiNola, A.; Haak, J. R. Molecular Dynamics with Coupling to an External Bath. J. Chem. Phys. 1984, 81 (8), 3684–3690. https://doi.org/10.1063/1.448118.

44. Thompson, A. P.; Aktulga, H. M.; Berger, R.; Bolintineanu, D. S.; Brown, W. M.; Crozier, P. S.; in 't Veld, P. J.; Kohlmeyer, A.; Moore, S. G.; Nguyen, T. D.; Shan, R.; Stevens, M. J.; Tranchida, J.; Trott, C.; Plimpton, S. J. LAMMPS - a Flexible Simulation Tool for Particle-Based Materials Modeling at the Atomic, Meso, and Continuum Scales. Comput. Phys. Commun. 2022, 271, 108171. https://doi.org/10.1016/j.cpc.2021.108171.

45. Glielmo, A., Zeni, C. & De Vita, A. Efficient nonparametric n-body force fields from machine learning. Phys. Rev. B 97, 184307 (2018).

46. Xie, Y.; Vandermause, J.; Sun, L.; Cepellotti, A.; Kozinsky, B. Bayesian Force Fields from Active Learning for Simulation of Inter-Dimensional Transformation of Stanene. Npj Comput. Mater. 2021, 7 (1), 1–10. https://doi.org/10.1038/s41524-021-00510-y.

47. Nosé, S. A Molecular Dynamics Method for Simulations in the Canonical Ensemble. Mol. Phys. 1984, 52 (2), 255–268. https://doi.org/10.1080/00268978400101201.

48. Nosé, S. A Unified Formulation of the Constant Temperature Molecular Dynamics Methods. J. Chem. Phys. 1984, 81 (1), 511–519. https://doi.org/10.1063/1.447334.

49. Hoover, W. G. Canonical dynamics: equilibrium phase-space distributions. Phys. Rev. A 31, 1695–1697 (1985).

50. Michaud-Agrawal, N.; Denning, E. J.; Woolf, T. B.; Beckstein, O. MDAnalysis: A Toolkit for the Analysis of Molecular Dynamics Simulations. J. Comput. Chem. 2011, 32 (10), 2319–2327. https://doi.org/10.1002/jcc.21787.

51. Gowers, R. et al. MDAnalysis: A python package for the rapid analysis of molecular dynamics simulations. in 98–105 (Austin, Texas, 2016). doi:10.25080/Majora-629e541a-00e.

52. Davies, M., Reyes-Figueroa, A. D., Gurtovenko, A. A., Frankel, D. & Karttunen, M. Elucidating lipid conformations in the ripple phase: machine learning reveals four lipid populations. Biophys. J. 122, 442–450 (2023).

53. Sukhomlinov, S. V. & Müser, M. H. A mixed radial, angular, three-body distribution function as a tool for local structure characterization: application to single-component structures. J. Chem. Phys. 152, 194502 (2020).

54. Wang, Z., Bovik, A. C., Sheikh, H. R. & Simoncelli, E. P. Image quality assessment: from error visibility to structural similarity. IEEE Trans. Image Process. 13, 600–612 (2004).

55. Van Der Maaten, L. & Hinton, G. Visualizing data using t-SNE. J. Mach. Learn. Res. 9, 2579–2605 (2008).

56. Schubert, E., Sander, J., Ester, M., Kriegel, H. P. & Xu, X. DBSCAN revisited, revisited: why and how you should (still) use DBSCAN. ACM Trans Database Syst 42, 19:1-19:21 (2017).

57. Johannsmann, D. The Quartz Crystal Microbalance in Soft Matter Research, 1st ed.; Soft and Biological Matter; Springer: Switzerland, 2015.